COMMUNICATION

Check for updates

An in-sensor humidity computing system for contactless human–computer interaction†

Meng Qi, [ID] ‡[a] Runze Xu,‡[a] Guanglong Ding,[b] Kui Zhou,[b] Shirui Zhu,[a] Yanbing Leng,[a] Tao Sun,[a] Ye Zhou [ID] [b] and Su-Ting Han [ID] *[c]

Being capable of processing large amounts of redundant data and decreasing power consumption, in-sensor computing approaches play significant roles in neuromorphic computing and are attracting increasing interest in perceptual information processing. Herein, we proposed a high performance humidity-sensitive memristor based on a Ti/graphene oxide (GO)/HfO$_x$/Pt structure and verified its potential for application in remote health management and contactless human–machine interfaces. Since GO possesses abundant hydrophilic groups (carbonyl, epoxide, and hydroxyl), the memristor shows a high humidity sensitivity, fast response, and wide response range. By utilizing the proton-modulated redox reaction, humidity exposure to the memristor induces a dynamic change in the switching between high and low resistance states, ensuring essential synaptic learning functions, such as paired-pulse facilitation, spike number-dependent plasticity, and spike amplitude-dependent plasticity. More importantly, based on the humidity-induced salient features originating from the abundant hydrophilic functional groups in GO, we have implemented a noncontact human–machine interface utilizing the respiratory mode in humans, demonstrating the potential of promoting health monitoring applications and effectively blocking virus transmission. In addition, the high recognition accuracy of contactless handwriting in a 5 × 5 array artificial neural network was successfully achieved, which is attributed to the excellent emulated synaptic behaviors. This study provides a feasible method to develop an excellent humidity-sensitive memristor for constructing efficient in-sensor computing for application in health management and contactless human–computer interaction.

[a] *Institute for Microscale Optoelectronics, Shenzhen University, Shenzhen 518060, P. R. China*

[b] *Institute for Advanced Study, Shenzhen University, Shenzhen 518060, P. R. China*

[c] *Department of Applied Biology and Chemical Technology, The Hong Kong Polytechnic University, Hong Kong, China. E-mail: suting.han@polyu.edu.hk*

† Electronic supplementary information (ESI) available. See DOI: https://doi.org/10.1039/d3mh01734f

‡ M. Qi and R. Z. Xu contributed equally to this work.

New concepts

A new-type of humidity-sensitive memristor is constructed based on the structure of Ti/GO/HfO$_x$/Pt, which has potential for use in health management and contactless human machine interfaces. Using moisture-electric annealing, GO not only acted as a center for the accumulation of water molecules, but also induced the formation of internal electrical field. This induced electrical field both accelerated the movement of O^{2-} and increased the conductance of the memristor, which made it possible to modulate the migration of O^{2-} to mimic the plastic behaviors, such as paired-pulse facilitation, spike number-dependent plasticity, and spike amplitude-dependent plasticity, making it inherently more biological. This device can be further controlled by utilizing respiratory stimulation, indicating its potential for application in health management. In addition, the humidity-sensitive memristor successfully demonstrated excellent contactless handwriting in an artificial neural network. The proposed approach has potential to provide novel platforms for the development of artificial sensory neurons, which is of great significance for non-contact human–computer interaction in intelligence applications.

Introduction

Humidity is one of the most essential physiological indicators, which play key roles in health management and contactless human machine interfaces, holding great potential to revolutionize state-of-the-art lifestyle.[1–4] For instance, monitoring the parameters of respiration, including the rhythm,[5,6] frequency,[7] and intensity,[8] is extremely useful to diagnose heart diseases and prevent respiratory failure. Nevertheless, most of the reported humidity sensor systems have separate humidity sensors for collecting sensory information as the analogue signal, analogue-to-digital conversion (ADC) to transform data into digital form, a memory unit to store the information, and processing units to retrieve data for further calculation (Fig. 1a).[9–12] The complicated circuit design and system construction require sophisticated integration techniques,[13] which also increase the latency and computing power of the overall system,[14,15] inevitably influencing the efficiency, esthetics, and comfort of the system.[13–16]
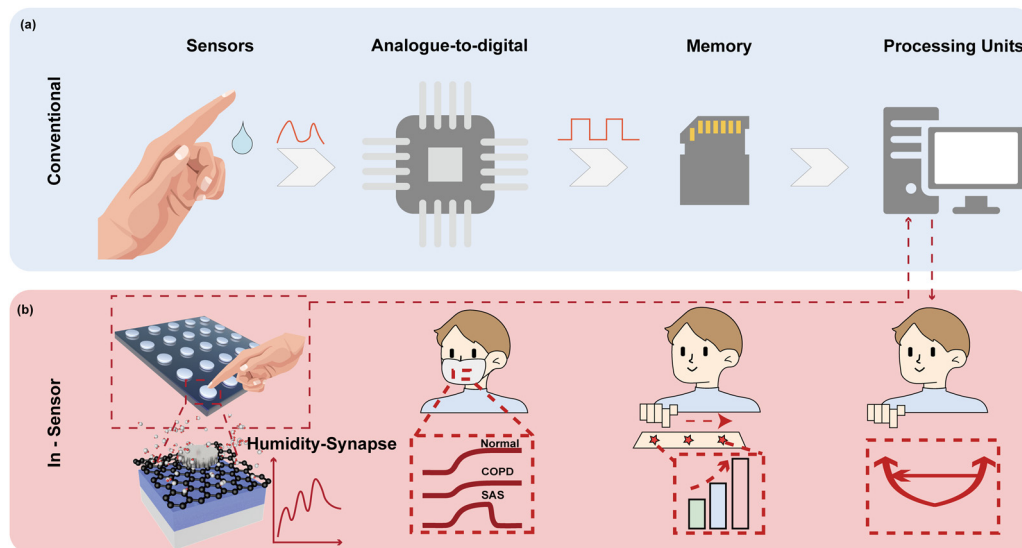
Fig. 1 (a) The architecture of conventional sensors. Sensor outputs (analog signals) are first converted into digital signals (generated by an ADC chip) and stored in memory. The processing unit loads the data from the memory, and then transfers output signals back to the memory for storage. (b) The architecture of in-sensor computing with both sensing and storage capabilities; data can be transmitted directly to the processing unit, eliminating intermediate redundant steps.

Inspired by the biological perception system with a data-centric tactic, in-sensor computing architectures bring an innovative concept to improve the evaluation efficiency of humidity-indicated health management because the sensory data can be locally filtered, memorized, and processed without shuttling.[14,17–19] Stimuli in the form of humidity bind to receptor cells to generate action potentials, which induce the release of neurotransmitters from the receptor cells to afferent neurons for further processing.[20–22] For in-sensor computing, an intelligent device should be capable of simultaneously sensing, filtering, memorizing, and processing the humidity signal at the device level.[22–26] In addition, the dynamic response in various humidity environments with a high sensitivity, fast speed, and long-term memory is highly demanded. Two-terminal memristors are especially suitable for in-sensor computing because of their several advantageous features of inherent dynamics, including a high speed switching,[27,28] low energy consumption,[29,30] high-density integration,[31] and scalability.[32,33] The conductivity of memristor encoded sensory information serves as synaptic weights.[34,35] By collecting the cumulative output conductance of the memristor in a cross array, matrix vector multiplication can be accomplished in a single clock cycle taking advantage of the Ohm's law and Kirchhoff's law.[36–39] Hence, high parallelism can be easily obtained with reduced latency and power consumption. However, traditional memristors based on a metal oxide switching layer exhibit low sensitivity to humidity since water is inadequate for driving the migration of anions in the resistive switching layer.[1,40,41] Integrating the materials with highly hydrophilic nature and pronounced conductance changes upon humidity variation as the switching layer of memristors is expected to achieve controllable physicochemical behavior under adsorption/desorption of water molecules.

In this work, a high-performance humidity-sensitive memristor was proposed with the structure of Ti/graphene oxide (GO)/HfO$_x$/Pt and was simultaneously verified to have the capability for application in remote health management and contactless human–machine interface. Since GO possesses abundant hydrophilic groups (carbonyl (C=O), epoxide (C–O–C), and hydroxyl (C–OH)),[1,42,43] the memristor shows high humidity sensitivity (795.31%, C$_{90\%\text{ relative humidity (RH)}}$/C$_{40\%\text{RH}}$ × 100%), fast response (0.1 s), and a wide response range (20% to 95%) (for details, see Note 1 in the ESI†).[1,44] In addition, the humidity exposure of the memristor evokes the dynamic change in switching between the high conduction state (HRS) and low conduction state enabled via proton-modulated redox reaction, ensuring the possibility of synaptic functions imitated such as paired-pulse facilitation (PPF), spike number-dependent plasticity (SNDP), and spike amplitude-dependent plasticity (SADP). Based on the multifunctionality and reconfigurability of the memristor, we further design an integrated array to demonstrate its applications in respiratory monitoring systems and contactless gesture recognition systems.

Experimental details

Materials

Graphene oxide (1 mg mL^{-1}) was purchased from MK NANO Co., LTD. The precursor used for atomic layer deposition is TDMA-Hf, which was purchased from Jiaxing Kemicro Electronic Equipment Co., Ltd. Ti target (99.99%) and Pt target (99.99%) were purchased from Fuzhou Innovation Photoelectric Technology Co., LTD. A P-type silicon substrate with 300 nm SiO$_2$ was purchased from Suzhou Crystal Silicon Electronic & Technology Co., Ltd.

GO/HfO$_x$ sensory memristor fabrication

The 5 nm Ti and 50 nm Pt bottom electrode (BE) were orderly deposited on the SiO$_2$ substrate by magnetron sputtering using a metal Pt/Ti target. The 15 nm HfO$_x$ film was prepared by atomic layer deposition (ALD) using argon with a pressure of 0.15 torr at 200 °C. Subsequently, the surface of the HfO$_x$ film was treated using an ultraviolet ozone cleaner for 30 minutes, and then the graphite oxide dispersion was prepared on the surface of the HfO$_x$ film by the spin coating method at 1000 rpm for 10 s. The sample was baked at 40 °C for 1 h to remove any remaining solvents. Finally, 50 nm top electrodes (TEs) with a diameter of 300 μm with the use of a shadow mask were deposited on the sample by magnetron sputtering.

Characterization

Surface elemental analysis was performed by X-ray photoelectron spectroscopy (XPS) and the topography of the device was measured by atomic force microscopy (AFM). The DC-based electrical and pulse measurements were performed using an Agilent B1500A semiconductor parameter analyzer. The various humidity conditions were established through a sealed metal box containing a humidifier and a hygrometer. An impedance analyzer was employed for recording AC complex impedance spectroscopy using the frequency scanning mode with a frequency range from 100 Hz to 1 MHz.

Results and discussion

Inspired by the biological sensory system, an in-sensor humidity computing system was constructed for achieving a high-performance diagnostic system of respiratory disease and a contactless gesture recognition system (Fig. 1b). In the human sensory system, senses, transmission and recognition of the humidity signal depend on the parallel networks of sensory neurons, nerves and the cerebral cortex.[45–47] The humidity signals are received by the sensory neurons and then conveyed along synapses and neurons as a form of spike to the cortex that performs memory, learning, and recognition functions.[47,48] Thus, different from the traditional diagnostic system for latency humidity recognition, the multifunctional and configurable memristor-based system is capable of sensing, memorizing and processing parallelly to ensure high energy efficiency and accuracy.

Fig. 2a illustrates the schematic of the proposed memristor with the structure of Ti/GO/HfO$_x$/Pt. The Ti as the adhesion layer and Pt as the BE were orderly deposited on the SiO$_2$ substrate by magnetron sputtering. A 15 nm HfO$_x$ film was then manufactured by ALD. GO nanosheets were prepared according to the Hummers' method presented in the previous report.[49] Subsequently, the well dispersed GO solution was spin-coated the surface of the HfO$_x$ film to form a densely packed GO film. Finally, 50 nm Ti TEs with a diameter of 300 μm were deposited on the switching layer. Details of the fabrication process of the
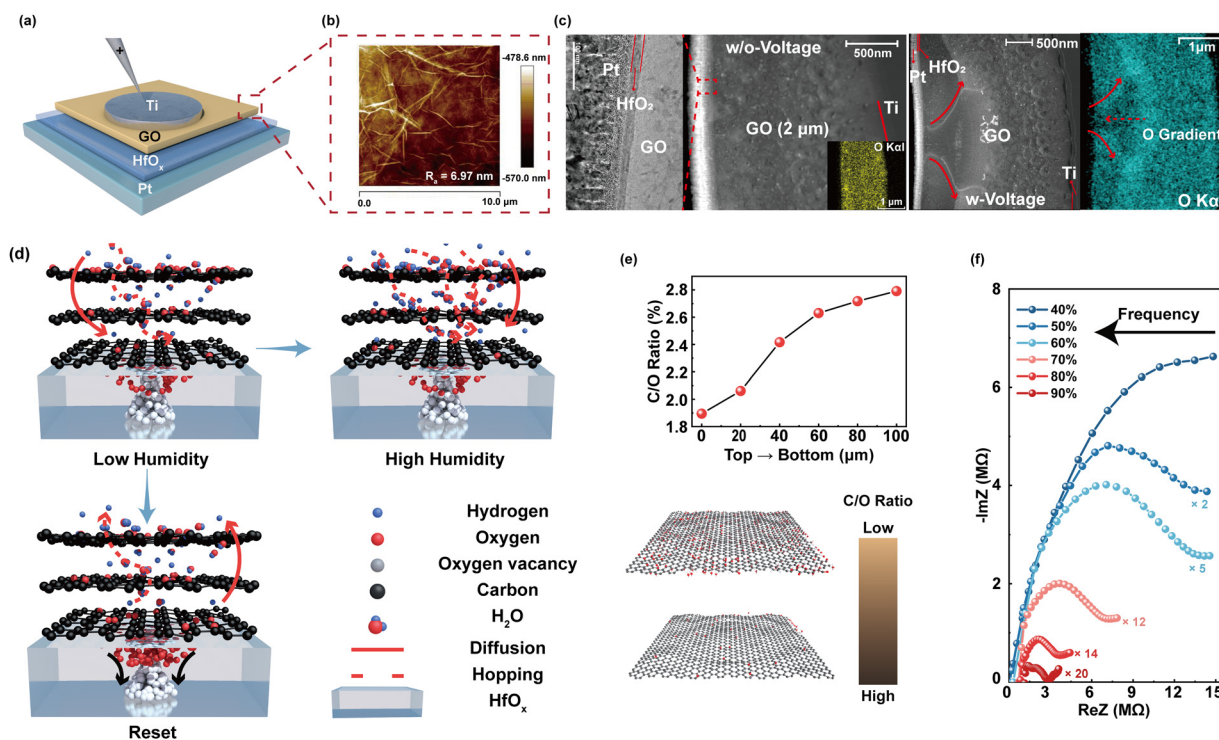

Fig. 2 (a) A schematic illustration of the GO/HfO$_x$ sensory memristor. (b) The surface morphology of the GO film displayed by AFM. (c) The cross-sectional TEM images of the Pt/HfO$_x$/GO/Ti structure (left: without voltage, right: with voltage). (d) A schematic illustration of hopping H$^+$ and diffusion mechanism with various humidity in the GO film and the generation of Vo in the HfO$_x$ film. (e) The C/O atomic ratio of the GO film in the vertical direction from top to bottom calculated by XPS spectra. (f) The AC complex impedance plots of the GO film at various RH levels (40%–90% RH).

memristor are described in the Methods section. The AFM images show that the single GO sheet exhibits a flat surface and small roughness of R_a = 6.97 nm (Fig. 2b). Fig. 2c depicts the cross-sectional transmission electron microscope (TEM) image and energy-dispersive spectroscopy (EDS) of GO-HfO$_x$, where the continuous surface of each layer was verified. As a comparison, the corresponding EDS mapping of O in the region before and after the action of the electric field is recorded. Obviously, the appearance of oxygen gradient originates from the electrical treatment of the GO layer. There is no different contrast in the top region of GO, which may be responsible for adsorbing and retaining water.[42,43]

Fig. 2d depicts the working mechanism of the GO-HfO$_x$ memristor, which can be well controlled *via* the proton sources by changing the RH. By application of a positive bias on the Ti TE, oxygen ions (O^{2-}) dissociate from HfO$_x$ and migrate from the Pt BE towards the Ti TE under an external electric field, giving rise to the growth of oxygen vacancy (Vo) conductive filaments (CFs) in the HfO$_x$-GO layer with the gradual increase of oxygen content from the TE to the BE.[50–52] Under exposure to humidity, the GO film adsorbs water molecules owing to its oxygen-containing groups with strong hydrophilicity (*e.g.*, –OH and –COOH) and this strategy is defined as moisture-electric annealing.[43] The accumulation of water molecules in the O-rich region of GO films induces the regional solvation effect, which further breaks the O–H bond to release free protons (H$^+$).[42,43] The free H$^+$ further migrate from the TE towards the BE along

the oxygen gradient in the GO film and induce the formation of internal electrical field. This induced electrical field tends to accelerate the migration of O^{2-} and establishment of Vo CFs, which further increases the conductance of the memristor. Thus, our HfO$_x$-GO memristor can emulate the humidity-modulated plastic behavior of sensory synapse with increased RH.

The atomic ratio (C/O) of the as-deposited GO film after moisture-electric annealing was investigated by XPS (see Fig. S1 in the ESI† for more details). As summarized in Fig. 2e, the C/O atomic ratio gradually increases along the direction of the electric field, indicating the reduction of GO. Further, humidity-controlled electrical behaviors were investigated by complex impedance spectroscopy (CIS). Fig. 2f shows the CIS of the GO humidity sensor under different RH levels from 40% to 90%. At a lower RH of 40%, the larger curvature radius of the curve in the CIS plot stemming from the intrinsic impedance of the sensing film can be observed. According to Anderson's proton conductivity model, the hydrophilic group (*i.e.*, C–O–C) of GO can only absorb a small amount of water molecules in this case; thus, the surface is not completely covered by water to release fewer H$^+$.[42,53] With increasing humidity RH from 60% to 90%, a portion of a semicircle gradually appears in the CIS curve, and moreover, the higher RH (60%–90%) results in a more obvious linear behavior on the curved tail wing, indicating that the intrinsic impedance decreases with increased RH, which may be attributed to the release of H$^+$.[53,54] As a result, the phenomenon of dependence of conductivity on humidity has
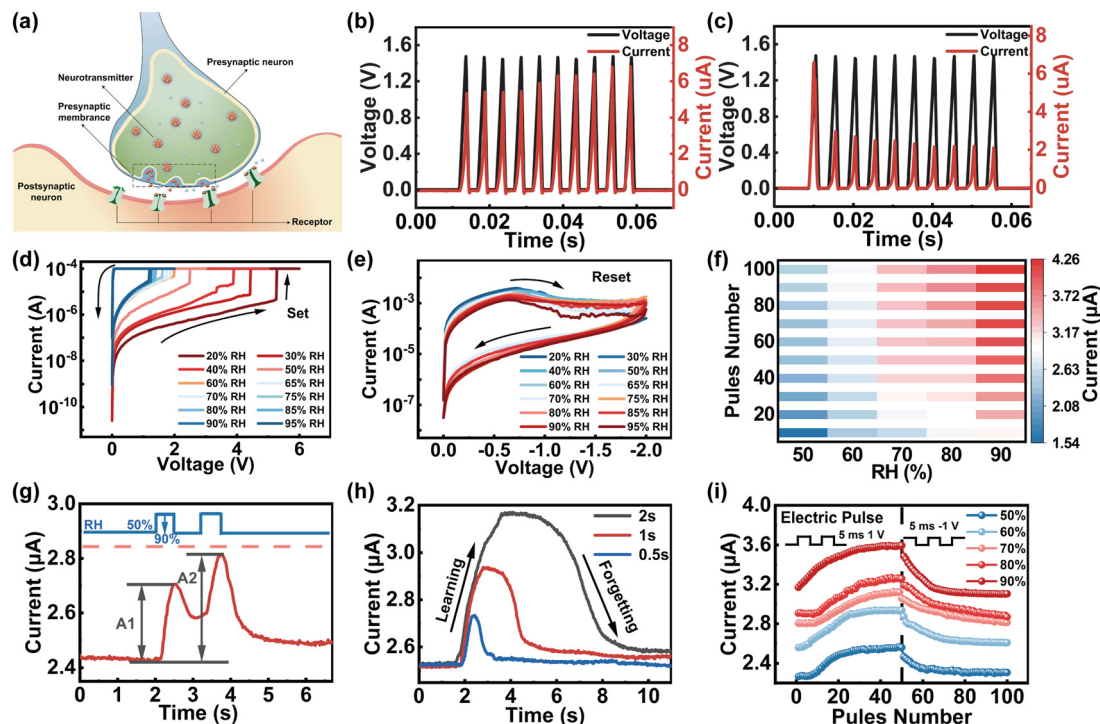

Fig. 3 (a) A schematic illustration of the biological synapse. Current and voltage as a function of time for the GO/HfO$_x$ memristor in (b) positive voltage pulse and (c) negative voltage pulse. (d) The SET process and (e) RESET process of the GO/HfO$_x$ sensory memristor with various RH (20–95%). (f) The current variation of the GO/HfO$_x$ memristor at various RH (50–90%, amplitude: 1 V, duration: 5 ms). (g) The PPF behavior triggered by two consecutive humidity pulses (RH from 50% to 95%, 1 s). (h) Current response under the RH of 95% with various humidification durations. (i) The gradual current change of the GO/HfO$_x$ memristor with 50 voltage pulses (+1 V for potentiation, −1 V for depression) with various RH (50–90%).

great potential for a humidity-sensitive memristor for the applications of health monitoring and contactless human–machine interaction.

To understand the synaptic properties of our memristor under humidity stimuli, the Ti/GO/HfO$_x$/Pt memristor was employed to emulate the basic synaptic functions including PPF, SNDP, SADP, and spike duration-dependent plasticity (SDDP) of biological humidity synapse. Fig. 3a schematically illustrates the biological synapse that connects pre- and post-synaptic neurons where the connection strength of the synapse can respond dynamically under moisture stimulus (i.e., synaptic plasticity), standing for the neurochemical basis of learning and memory. The TE/BE of the memristor can be functionally considered as presynaptic/postsynaptic neurons, the RS layer serves as a synaptic gap and the continuously controlled conductivity of the memristor is analogous to synaptic plasticity. The continuous modulation of conductance states was first demonstrated by applying the train of 10 voltage pulses with an amplitude of 1.5 V, duration of 5 ms and interval of 5 ms on the device under a fixed ambient RH of 40%, as shown in Fig. 3b and c. The current of the GO/HfO$_x$ memristor increases/decreases gradually under positive/negative sweeps, which is a synaptic memristor. Then, with the fixed positive/negative voltage scan from 0 V to 6 V to 0 V (Fig. 3d), the ambient moisture could be used as a stimulus to modulate the set voltage (V_{SET}) of the memristor from $\sim$5.2 V to $\sim$1.2 V with RH increasing from 20% to 95%. In addition, the resistance of

the HRS decreases with the increased RH value. The statistical data of stability and reliability is shown in the ESI† (Fig. S2). When the negative sweep voltage was applied from 0 V to -2 V to 0 V (Fig. 3e), the negative differential resistance effect of decreasing current with increasing voltage was observed since the switching channel changes from fast Vo CFs to slow proton conductive CFs.

It is well established that the synaptic plasticity in biology could be affected by the frequency, intensity, and duration of stimuli;[55,56] thus, the modulation of pulse interval time, amplitude and duration time is deliberate on the humidity-sensitive memristor for modulating the conductance. As shown in Fig. 3f, greater variations in conductivity could be attained with the increase of humidity (RH $\sim$ 50% $\rightarrow$ RH $\sim$ 90%; 1 V, 5 ms), which is consistent with the biological synaptic behavior (for more details, see Fig. S3, ESI†).[26,57,58] Furthermore, the PPF function with correlations between the temporal spike pair was further investigated in response to the humidity stimulus (for detailed PPF information, see Fig. S4, ESI†).[59,60] As presented in Fig. 3g, excitatory postsynaptic current (EPSC) as the foundation of synaptic weight on the variation was evoked by monitoring the response to two moisture pulses with RH values of 50% and 95%, duration of 0.5 s and interval of 0.5 s. The second moisture pulse (RH $\sim$ 95%) arrives before the complete disappearance of the first EPSC, which accelerates the diffusion and accumulation of H$^+$ within GO, leading to higher conductance changes. Thus, the peaks of EPSC excited by the second
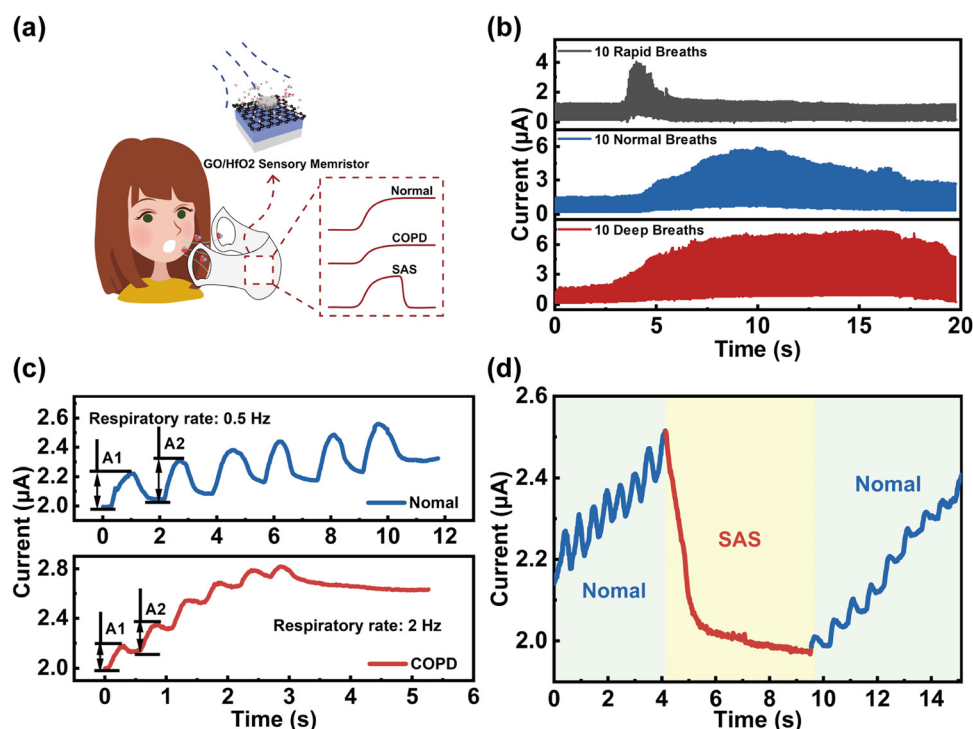

Fig. 4 (a) A schematic illustration of the respiratory detection module based on the GO/HfO$_x$ memristor. (b) Response currents detected by the GO/HfO$_x$ memristor with 10 breaths for different respiratory ways (grey: rapid breath, blue: normal breath, and red: deep breath). (c) Comparison of respiratory humidity between COPD patients and normal people (blue: normal people's breath and red: COPD patient's breath). (d) The typical respiratory signals of SAS patients (blue: normal respiratory signal and red: SAS patient respiratory signal).

moisture pulse (A2) were obviously larger than that of the first pulse (A1). The higher EPSC in Fig. 3h reflects the remarkable synaptic enhancements through a larger humidity pulse width (0.5 s, 1 s, and 2 s), while it takes longer to recover the final state after removing the humidity pulse (RH range from 90% to 50%) representing the long-term memory effect of the human brain. In order to emulate long-term potentiation characteristics under modulation of RH, a pulse train of 50 electrical pulses with an amplitude of 1 V/−1 V and duration of 5 ms were applied as the presynaptic spikes (Fig. 3i). The nonlinearity is calculated to be 1.70768 (50%RH), 1.54824 (60% RH), 1.03238 (70% RH), 1.0209 (80% RH), 2.78658 (90% RH), which is the key parameter for a synapse to the realization of weight updating approach to high-level in-sensor computing (see ESI,† Note 2, for discussion of nonlinearity).[61–63] The above results indicate that the reported humidity-sensitive memristor may be in accord with the characteristics of artificial synapses and provide a feasible strategy for the development of neuromorphic sensors for artificial intelligence.

We further expanded the application in respiratory monitoring systems by utilizing humidity sensitive memristors since many respiratory diseases including bronchitis, pneumonia, respiratory disturbance syndrome (SAS), and chronic obstructive pulmonary disease (COPD) are life-threatening. Fig. 4a shows the schematic diagram of an integrated respiratory monitoring system based on our memristor which can sense, memorize and process respiratory data (*i.e.*, normal, COPD, and SAS) simultaneously. First, the current of the memristor was recorded with application of moisture-encoded ventilation mode including rapid, normal, and deep breathing of healthy people from exercise, normal, and relaxation states, as shown in Fig. 4b. From the slow-breathing rate of ∼12 per minutes to a fast-breathing rate of up to ∼120 breaths per minute (blue line), the memristor exhibits highly distinguished current responses with different delay times, frequencies and amplitudes. Moreover, the current response is strongly distinguishable between healthy people and patients with respiratory diseases. For example, the patients with COPD exhale drier gas than normal healthy people within one breath since the airway and throat of COPD patients is permanently blocked. In addition, the inspiratory and expiratory time of patients with COPD will be significantly lower than that of healthy humans, while the inspiratory flow will be remarkably restricted because of bronchospasm, *etc.* Therefore, detecting and processing various respiratory parameters of samples *via* our memristor can effectively differentiate between COPD patients and healthy people. In the breathing scheme, moisture pulses with a RH of 90%/RH of 80% and duration of 50 ms are utilized to mimic the breath of healthy people/COPD patients for implementing respiratory stimuli on the device, as illustrated in Fig. 4c. The output current responses caused by external stimuli in identical directions are distinguishing. Current spikes with a high rate (2 Hz) and amplitude variation (0.2281 μA) to achieve saturation state is biologically analogous to the case of COPD patients because their respiratory rate is relatively faster. Compared to the feedback from COPD patients, the current spikes of healthy people are at lower rate

(0.5 Hz) with amplitude variation (0.1671 μA). Furthermore, the potential application of the humidity-sensitive memristor based respiratory monitoring system for monitoring SAS function is demonstrated in Fig. 4d. The typical current response of SAS patients was recorded by application of 1 V voltage, where the blue and red markers represent the signals of normal breathing and apnea, respectively. As shown, the apnea process correlates with a smaller current level compared with normal breathing, which is a great impetus to the diagnosis of apnea syndrome.

Besides the respiratory monitoring, we designed a 1 × 3 crossbar array of the humidity-sensitive memristor for the application of a gesture recognition system to address the motion of fingers by combining time coding effect. Different humidity fields of skin with a RH range from ∼98% to ∼45% can be induced by distance modulation from 2 mm to 10 mm between fingers and devices (Fig. 5a, schematic of finger movement in the insets of Fig. 5a). Fig. 5b presents the post-synaptic currents (PSCs) as a function of finger movement time. With the finger approaching the memristor, the moving signal can be detected as a presynaptic spike to generate current output with an amplitude of approximately 14.68 μA and saturation time (ST) of 1.13 s, respectively. To further investigate the distance correlation of the PSC/ST, the peak current/response time (RT) was collected and compared, as shown in Fig. 5c. It is worthwhile mentioning that the humidity synaptic device with memory effect is capable of generating current that is inversely proportional to the distance changes. The PSC/ST variation range from 14.68 μA to 2.48 μA/1.13 s to 3.54 s can be modulated by approaching distance from 2 mm to 10 mm, providing the basis for recognition of gestures.

Furthermore, we utilized a 1 × 3 memristor array to sense and process humidity information by decoding the distance between the finger and the device as well as the direction of finger movement, as shown in Fig. 5d. The noncontacting finger motions including drawing left, drawing right, enlargement, and shrinking can be recognized by the gesture recognition system. By collecting the humidity information from the memristor at different grid points, the feature vector was constructed depending on the onset time, which can be expressed as $T = [t_a, t_b, t_c]$. The detected signal current vector can be expressed as $P = [\text{PSC}_a, \text{PSC}_b, \text{PSC}_c]$. When the longitudinal spacing is fixed, the amplitude of output current correlates with the RH, which varies with increased distance between the finger and device. The vector concatenate of T and P provides the six-dimensional vectors $F = [w_a, w_b, w_c, \text{PSC}_a, \text{PSC}_b, \text{PSC}_c]$ ($w = t_{\text{spiking}}/t_{\text{movement}} \times 100\%$) as the input vector. F vector is first collected from the memristor array and then fed into a software-simulated fully connected artificial neural network (ANN) with six inputs and four outputs for final recognition, in which the input neurons are connected with 12 hidden neurons. The conjugate gradient backpropagation of Fletcher–Reeves was utilized as the weight update algorithm (see ESI,† Note 3, for discussion of the algorithm).[64] Fig. 5e shows a flowchart of the perception learning using the ANN computing process. The learning steps are described as follows: (1) input
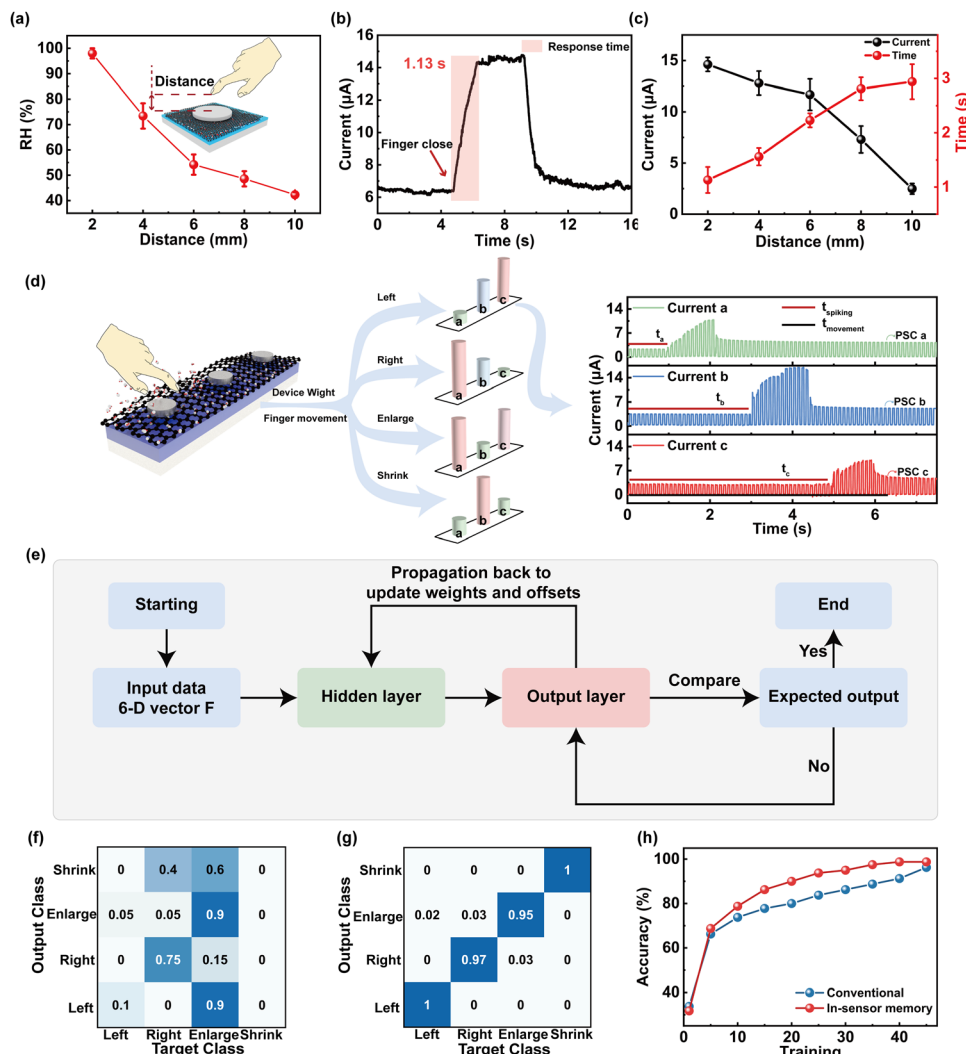
Fig. 5 (a) The dependence of RH on finger distance above the GO/HfO$_x$ sensory memristor. (b) RT of the GO/HfO$_x$ memristor sensing an approaching finger. (c) Response currents and RT of the finger at different distances above the GO/HfO$_x$ memristor. (d) The ratio of that *trig* time of the GO/HfO$_x$ memristor to the total motion time of the finger in different motion tracks of the finger and the response currents of the corresponding three devices in the ''left movement'' motion of the finger. (e) A flowchart of conjugate gradient backpropagation of the Fletcher–Reeves update–based neural network computing process. The confusion graph of output and target for the first training cycle (f) and 45th training cycle (g). (h) The accuracy of finger motion trajectory recognition.

data is fed into the input layer (*F*, as the input data); (2) the activation function of sigmoid is utilized to transfer data from the hidden layer to the output layer; (3) the median error between the network output data and the actual data is calculated; (4) the loss and gradient is calculated by using the gradient descent algorithm for minimizing losses; (5) the ΔW is updated (the updated value of the hidden layer weight). The learning process stops when the accuracy is greater than 99% or the accuracy is not improved after 5 times continuous iteration. The system returns to step 2 to implement the next iteration if the end condition was not reached. The confusion graph for the 1st and 45th recognition is, respectively, shown in Fig. 5f and g. The confusion matrix for 4 labels of the target class and output class is validated. After the 1st training, the label ''left'' is only 10% correctly recognized (Fig. 5f), while the correct recognition

rate of that after the 45th training is 100% (Fig. 5g). In contrast to the conventional calculation methods, higher recognition accuracy (98.75%) after 45 training epochs is displayed in Fig. 5h.

Next, we have implemented a feature extraction and learning architecture that provides a new strategy for sensing and processing technology. A typical ANN utilizing a fully connected method was established for performing the handwriting recognition with a finger close to the device in a 1 cm device spacing, as shown in Fig. 6a and b. An ANN schematic image consisting of the humidity-memristive synapse 5 × 5 arrays with three neuron layers (25 input neurons × 40 hidden neurons × 26 output neurons) is shown in Fig. 6a. The input information is transmitted to a neural network classifier *via* the PSC and pre-synaptic current (PrSC). Conductance variations are used as the
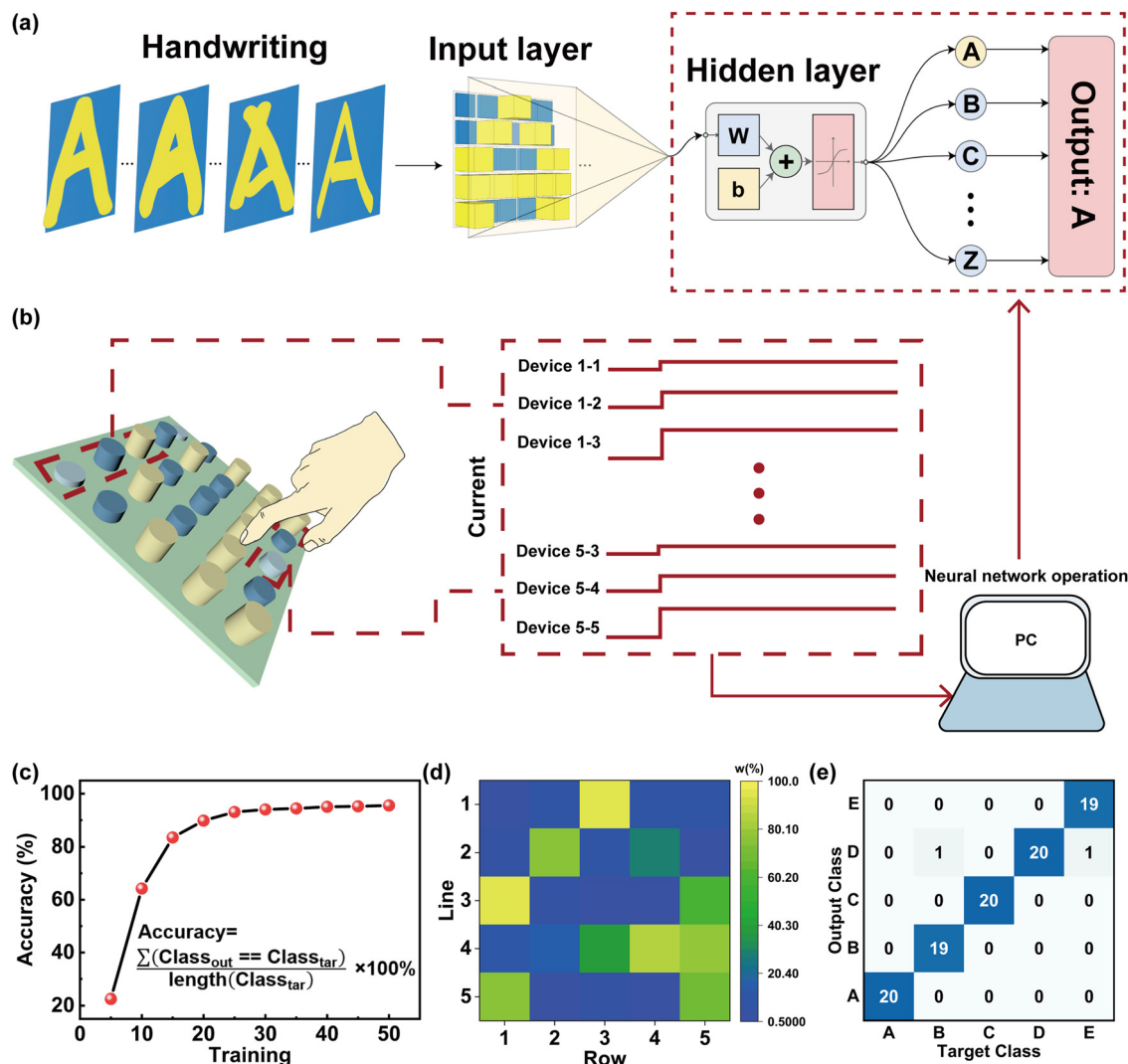
Fig. 6 (a) A schematic of handwriting recognition based on in-sensor computing. (b) The structure and working principle of the humidity in-sensor handwriting recognition system. (c) The accuracy of handwriting recognition. (d) The weight of 5 × 5 array after handwriting. (e) The confusion graph of the output class and the target class about handwriting letters of alphabet "A," "B," "C," "D," and "E" after 40 cycles.

input layer of the ANN (defined as $W = (PSC - PrSC)/PSC \times 100\%$). The W of each memristor can reflect the input trajectory of handwritten letters, which is related to the distance of fingers from the device (Fig. 6b). It is worth mentioning that the entire system has a near-sensor computing architecture, which can be used for real-time humidity collection and detection of finger-proximity patterns. The training process for handwritten letter recognition is performed based on conjugate gradient backpropagation with Fletcher–Reeves updates and the recognition accuracy is displayed in Fig. 6c.[64,65] During the backpropagation process, the weights were updated in the repeated epochs of training until the error was decreased. Notably, the recognition accuracy of handwritten letters rapidly increased from 64.231% to 94.423% induced by the increase of iterations from 10 to 40 cycles and reached the saturation state. Fig. 6d shows the weights of each device in the 5 × 5 array for the recognition of the letter 'A' in the in-senor computing.

This is further supported by the noise of dataset for the training shown in the ESI† (Fig. S5). In this realization, the confusion graph building block for the construction of 'A' 'B' 'C' 'D' 'E' five letters from the alphabet of 26 different strokes or different curvatures of the same stroke is displayed in Fig. 6e. The recognition accuracy can still reach more than 94% (see Fig. S6 and S7 in the ESI† for more details). This result suggests that our sensing memristors have the capability for handwritten recognition with a high accuracy in ANNs.

Conclusions

In summary, we developed an in-sensor humidity computing system composed of a sensing memristor with a Ti/GO/HfO$_x$/Pt structure for handwriting recognition. The basic functions of synaptic plasticity with bearing resemblances to the biological

synapse were successfully obtained based on the Ti/GO/HfO$_x$/Pt device, including EPSC, PPF and STDP. In particular, the oxygen concentration gradients generated by electrical annealing with the action of humidity were responsible for dominating the electrokinetic effect. Further, the inputs of the humidity can be achieved by human respiration, and this result can be consistent with the characteristics of disease-free humans under exercise, normal, and relaxed conditions. In addition, the obtained sensing memristor demonstrated outstanding performance and could be used for contactless detection of humidity variation. Based on our system, the high recognition accuracy of handwriting matched the simulation results. The system achieved 94.423% recognition accuracy after 40 iterations and maintained 90% accuracy even under 15% background noise level. We believe that our study provides a feasible approach toward highly reliable sensing memory and opens up a new design of highly efficient in-sensor computing for health management and contactless human–computer interaction.

Author contributions

Su-Ting Han conceived this work. Meng Qi and Runze Xu designed, prepared, and tested the experiment. Shirui Zhu, Yanbing Leng, and Tao Sun helped with the experiment design. Guanglong Ding and Kui Zhou participated in the discussion of experimental results. Meng Qi and Su-Ting Han wrote the manuscript. Ye Zhou and Su-Ting Han supervised the project. All authors reviewed and commented on the manuscript.

Conflicts of interest

The authors declare no conflict of interest.

Acknowledgements

Notes and references

1 S. Li, Y. Zhang, X. Liang, H. Wang, H. Lu, M. Zhu, H. Wang, M. Zhang, X. Qiu, Y. Song and Y. Zhang, *Nat. Commun.*, 2022, **13**, 5416.

2 C. Yang, H. Wang, J. Yang, H. Yao, T. He, J. Bai, T. Guang, H. Cheng, J. Yan and L. Qu, *Adv. Mater.*, 2022, **34**, 2205249.

3 Y. Wang, L. Zhang, Z. Zhang, P. Sun and H. Chen, *Langmuir*, 2020, **36**, 9443–9448.

4 K. M. Willett, N. P. Gillett, P. D. Jones and P. W. Thorne, *Nature*, 2007, **449**, 710–712.

5 J. Dai, J. Meng, X. Zhao, W. Zhang, Y. Fan, B. Shi and Z. Li, *Adv. Mater. Technol.*, 2023, **8**, 2201535.

6 N. A. Baertsch, H. C. Baertsch and J. M. Ramirez, *Nat. Commun.*, 2018, **9**, 843.

7 Y. Li, C. Liu, H. Zou, L. Che, P. Sun, J. Yan, W. Liu, Z. Xu, W. Yang, L. Dong, L. Zhao, X. Wang, G. Wang and Z. L. Wang, *Cell Rep. Phys. Sci.*, 2023, **4**, 101191.

8 L. Ye, F. Wu, R. Xu, Z. Di, J. Lu, C. Wang, A. Dong, S. Xu, L. Xue, Z. Fan, L. Xu, K. Li, D. Li, A. Kursumovic, R. Zhao, R. Tang, L. Qiu, H. Wang, J. L. MacManus-Driscoll, Q. Jing, W. Li and H. Yang, *Nano Energy*, 2023, **112**, 108460.

9 M. Naqi, S. Lee, H. J. Kwon, M. G. Lee, M. Kim, T. W. Kim, H. K. Shin, S. Kang, S. Gandla, H. S. Lee, Y. Ahn, S. Lee and S. Kim, *Adv. Mater. Technol.*, 2019, **4**, 1900619.

10 W. Yang, W. Li, H. Lu, J. Liu and T. Zhang, *Sensors*, 2022, **22**, 7229.

11 Z. Wu, J. Yang, X. Sun, Y. Wu, L. Wang, G. Meng, D. Kuang, X. Guo, B. Du, C. Liang, X. Fang, X. Tang and Y. He, *Sens. Actuators, B*, 2021, **337**, 129772.

12 S. Kano and M. Fujii, *ACS Sustainable Chem. Eng.*, 2018, **6**, 12217–12223.

13 L. Sun, Z. Wang, J. Jiang, Y. Kim, B. Joo, S. Zheng, S. Lee, W. J. Yu, B.-S. Kong and H. Yang, *Sci. Adv.*, 2021, **7**, eabg1455.

14 F. Zhou and Y. Chai, *Nat. Electron.*, 2020, **3**, 664–671.

15 C. Liu, H. Chen, S. Wang, Q. Liu, Y.-G. Jiang, D. W. Zhang, M. Liu and P. Zhou, *Nat. Nanotechnol.*, 2020, **15**, 545–557.

16 C. Du, F. Cai, M. A. Zidan, W. Ma, S. H. Lee and W. D. Lu, *Nat. Commun.*, 2017, **8**, 2204.

17 Q. Hua, J. Sun, H. Liu, R. Bao, R. Yu, J. Zhai, C. Pan and Z. L. Wang, *Nat. Commun.*, 2018, **9**, 244.

18 Y. Liu, W. Yang, Y. Yan, X. Wu, X. Wang, Y. Zhou, Y. Hu, H. Chen and T. Guo, *Nano Energy*, 2020, **75**, 104930.

19 T. Wan, B. Shao, S. Ma, Y. Zhou, Q. Li and Y. Chai, *Adv. Mater.*, 2023, **35**, 2203830.

20 D. D. Frank, A. Enjin, G. C. Jouandet, E. E. Zaharieva, A. Para, M. C. Stensmyr and M. Gallio, *Curr. Biol.*, 2017, **27**, 2381–2388.

21 L. Liu, Y. Li, R. Wang, C. Yin, Q. Dong, H. Hing, C. Kim and M. J. Welsh, *Nature*, 2007, **450**, 294–298.

22 Y. H. Jung, B. Park, J. U. Kim and T. I. Kim, *Adv. Mater.*, 2019, **31**, 1803637.

23 T. Guo, J. Ge, Y. Jiao, Y. Teng, B. Sun, W. Huang, H. Asgarimoghaddam, K. P. Musselman, Y. Fang, Y. N. Zhou and Y. A. Wu, *Mater. Horiz.*, 2023, **10**, 1030–1041.

24 M.-K. Song, S. D. Namgung, Y.-W. Song, T. Sung, W. Ji, Y.-S. Lee, K. T. Nam and J.-Y. Kwon, *ACS Appl. Electron. Mater.*, 2021, **3**, 3372–3378.

25 H. Shao, Y. Li, W. Yang, X. He, L. Wang, J. Fu, M. Fu, H. Ling, P. Gkoupidenis, F. Yan, L. Xie and W. Huang, *Adv. Mater.*, 2023, **35**, 2208497.

26 J. Su, Y. Li, D. Xie and J. Jiang, *Mater. Horiz.*, 2023, **10**, 1745–1756.

27 K. Sun, J. Chen and X. Yan, *Adv. Funct. Mater.*, 2021, **31**, 2006773.

28 C. Li, M. Hu, Y. Li, H. Jiang, N. Ge, E. Montgomery, J. Zhang, W. Song, N. Dávila, C. E. Graves, Z. Li, J. P. Strachan, P. Lin,

Z. Wang, M. Barnell, Q. Wu, R. S. Williams, J. J. Yang and Q. Xia, *Nat. Electron.*, 2017, **1**, 52–59.

29 T. Zeng, X. Zou, Z. Wang, G. Yu, Z. Yang, H. Rong, C. Zhang, H. Xu, Y. Lin, X. Zhao, J. Ma, G. Zhu and Y. Liu, *Small*, 2021, **17**, 2006662.

30 C. Liu, X. Yan, X. Song, S. Ding, D. W. Zhang and P. Zhou, *Nat. Nanotechnol.*, 2018, **13**, 404–410.

31 P. Yao, H. Wu, B. Gao, J. Tang, Q. Zhang, W. Zhang, J. J. Yang and H. Qian, *Nature*, 2020, **577**, 641–646.

32 S.-O. Park, H. Jeong, J. Park, J. Bae and S. Choi, *Nat. Commun.*, 2022, **13**, 2888.

33 M. A. Zidan, J. P. Strachan and W. D. Lu, *Nat. Electron.*, 2018, **1**, 22–29.

34 P. M. Sheridan, F. Cai, C. Du, W. Ma, Z. Zhang and W. D. Lu, *Nat. Nanotechnol.*, 2017, **12**, 784–789.

35 C. Zhang, W. B. Ye, K. Zhou, H. Y. Chen, J. Q. Yang, G. Ding, X. Chen, Y. Zhou, L. Zhou, F. Li and S. T. Han, *Adv. Funct. Mater.*, 2019, **29**, 1808783.

36 D. Ielmini and H. S. P. Wong, *Nat. Electron.*, 2018, **1**, 333–343.

37 A. Sebastian, M. Le Gallo, R. Khaddam-Aljameh and E. Eleftheriou, *Nat. Nanotechnol.*, 2020, **15**, 529–544.

38 T. P. Xiao, C. H. Bennett, B. Feinberg, S. Agarwal and M. J. Marinella, *Appl. Phys. Rev.*, 2020, **7**, 031301.

39 J. Ma, H. Liu, N. Yang, J. Zou, S. Lin, Y. Zhang, X. Zhang, J. Guo and H. Wang, *Adv. Mater.*, 2022, **34**, 2202371.

40 Y. Zhang, Y. Chen, P. Westerhoff, K. Hristovski and J. C. Crittenden, *Water Res.*, 2008, **42**, 2204–2212.

41 H. S. Wong and S. Salahuddin, *Nat. Nanotechnol.*, 2015, **10**, 191–194.

42 Y. Yao, X. Chen, J. Zhu, B. Zeng, Z. Wu and X. Li, *Nanoscale Res. Lett.*, 2012, **7**, 363.

43 F. Zhao, H. Cheng, Z. Zhang, L. Jiang and L. Qu, *Adv. Mater.*, 2015, **27**, 4351–4357.

44 Z. Song, S. Li, B. Hou, Z. Cheng, Y. Xue and B. Chen, *IEEE Sens. J.*, 2023, **23**, 2291–2302.

45 H. Tan, Y. Zhou, Q. Tao, J. Rosen and S. van Dijken, *Nat. Commun.*, 2021, **12**, 1120.

46 J. Yu, Y. Wang, S. Qin, G. Gao, C. Xu, Z. Lin Wang and Q. Sun, *Mater. Today*, 2022, **60**, 158–182.

47 X. Zhang, Y. Zhuo, Q. Luo, Z. Wu, R. Midya, Z. Wang, W. Song, R. Wang, N. K. Upadhyay, Y. Fang, F. Kiani, M. Rao, Y. Yang, Q. Xia, Q. Liu, M. Liu and J. J. Yang, *Nat. Commun.*, 2020, **11**, 51.

48 W. Heng, S. Solomon and W. Gao, *Adv. Mater.*, 2022, **34**, 2107902.

49 H. Bi, S. Wan, X. Cao, X. Wu, Y. Zhou, K. Yin, S. Su, Q. Ma, M. Sindoro, J. Zhu, Z. Zhang, H. Zhang and L. Sun, *Carbon*, 2019, **143**, 162–171.

50 S. K. Kim, J. Y. Kim, B. C. Jang, M. S. Cho, S.-Y. Choi, J. Y. Lee and H. Y. Jeong, *Adv. Funct. Mater.*, 2016, **26**, 7406–7414.

51 S. Kumar, C. E. Graves, J. P. Strachan, E. M. Grafals, A. L. D. Kilcoyne, T. Tyliszczak, J. N. Weker, Y. Nishi and R. S. Williams, *Adv. Mater.*, 2016, **28**, 2772–2776.

52 C. Li, B. Gao, Y. Yao, X. Guan, X. Shen, Y. Wang, P. Huang, L. Liu, X. Liu, J. Li, C. Gu, J. Kang and R. Yu, *Adv. Mater.*, 2017, **29**, 1602976.

53 D. Zhang, J. Tong, B. Xia and Q. Xue, *Sens. Actuators, B*, 2014, **203**, 263–270.

54 L. Zhou, M. Wang, Z. Liu, J. Guan, T. Li and D. Zhang, *Sens. Actuators, B*, 2021, **344**, 130219.

55 Y. Park, M.-J. Park and J.-S. Lee, *Adv. Funct. Mater.*, 2018, **28**, 1804123.

56 Y. Park, M.-K. Kim and J.-S. Lee, *J. Mater. Chem. C*, 2020, **8**, 9163–9183.

57 L. Shan, H. Zeng, Y. Liu, X. Zhang, E. Li, R. Yu, Y. Hu, T. Guo and H. Chen, *Nano Lett.*, 2022, **22**, 7275–7283.

58 Y. Yan, Q. Chen, X. Wu, X. Wang, E. Li, Y. Ke, Y. Liu, H. Chen and T. Guo, *ACS Appl. Mater. Interfaces*, 2020, **12**, 49915–49925.

59 K. Wang, J. Liu, M. E. El-Khouly, X. Cui, Q. Che, B. Zhang and Y. Chen, *ACS Appl. Mater. Interfaces*, 2022, **14**, 36987–36997.

60 Z. Zhao, Q. Che, K. Wang, M. E. El-Khouly, J. Liu, Y. Fu, B. Zhang and Y. Chen, *iScience*, 2022, **25**, 103640.

61 Y. Wang, Y. Gong, L. Yang, Z. Xiong, Z. Lv, X. Xing, Y. Zhou, B. Zhang, C. Su, Q. Liao and S. T. Han, *Adv. Funct. Mater.*, 2021, **31**, 2100144.

62 J. Lee, B. H. Jeong, E. Kamaraj, D. Kim, H. Kim, S. Park and H. J. Park, *Nat. Commun.*, 2023, **14**, 5775.

63 M. Farronato, P. Mannocci, M. Melegari, S. Ricci, C. M. Compagnoni and D. Ielmini, *Adv. Mater.*, 2022, **35**, 2205381.

64 T.-T. Yao, Z.-J. Bai and Z. Zhao, *Numer Linear Algebra. Appl.*, 2019, **26**, e2221.

65 S. Pandey, D. A. Hindoliya and R. mod, *Sustainable Cities. Soc.*, 2012, **3**, 37–45.